



Determining the radial distribution function of water using electron scattering: A key to solution phase chemistry


Cite as: J. Chem. Phys. **153**, 194504 (2020); <https://doi.org/10.1063/5.0024127>

Submitted: 05 August 2020 . Accepted: 19 October 2020 . Published Online: 20 November 2020

 M. B. de Kock, S. Azim, G. H. Kassier, and  R. J. D. Miller

COLLECTIONS

 This paper was selected as Featured

 This paper was selected as Scilight



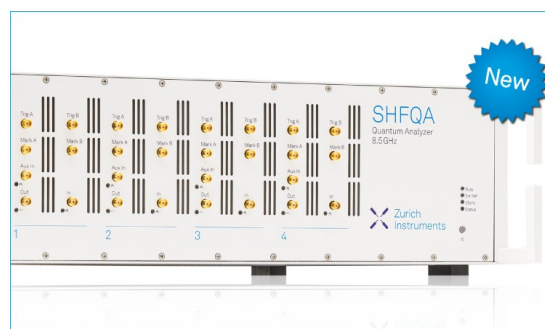
View Online



Export Citation



CrossMark



Your Qubits. Measured.

Meet the next generation of quantum analyzers

- Readout for up to 64 qubits
- Operation at up to 8.5 GHz, mixer-calibration-free
- Signal optimization with minimal latency

Find out more



Determining the radial distribution function of water using electron scattering: A key to solution phase chemistry



Cite as: J. Chem. Phys. 153, 194504 (2020); doi: 10.1063/5.0024127

Submitted: 5 August 2020 • Accepted: 19 October 2020 •

Published Online: 20 November 2020



View Online



Export Citation



CrossMark

M. B. de Kock,¹ S. Azim,¹ G. H. Kassier,¹ and R. J. D. Miller^{2,a)}

AFFILIATIONS

¹Max Planck Institute for the Structure and Dynamics of Matter, Luruper Chaussee 149, Bldg. 99 (CFEL), 22761 Hamburg, Germany

²Departments of Chemistry and Physics, University of Toronto, 80 St. George Street, Toronto, Ontario M5S 3H6, Canada

^{a)}Author to whom correspondence should be addressed: dmiller@lphys.chem.utoronto.ca

ABSTRACT

High energy electron scattering of liquid water (H₂O) at near-ambient temperature and pressure was performed in a transmission electron microscope (TEM) to determine the radial distribution of water, which provides information on intra- and intermolecular spatial correlations. A recently developed environmental liquid cell enables formation of a stable water layer, the thickness of which is readily controlled by pressure and flow rate adjustments of a humid air stream passing between two silicon nitride (Si₃N₄) membranes. The analysis of the scattering data is adapted from the x-ray methodology to account for multiple scattering in the H₂O:Si₃N₄ sandwich layer. For the H₂O layer, we obtain oxygen–oxygen (O–O) and oxygen–hydrogen (O–H) peaks at 2.84 Å and 1.83 Å, respectively, in good agreement with values in the literature. This demonstrates the potential of our approach toward future studies of water-based physics and chemistry in TEMs or electron probes of structural dynamics.

© 2020 Author(s). All article content, except where otherwise noted, is licensed under a Creative Commons Attribution (CC BY) license (<http://creativecommons.org/licenses/by/4.0/>). <https://doi.org/10.1063/5.0024127>

I. INTRODUCTION

The majority of known chemical and biological processes occur in a liquid medium. Hence, there is great interest in theoretical and experimental investigations of the liquid structure and its evolution at the molecular level.^{1,2} Water stands out in this regard owing to its ubiquity and many exceptional properties that have been extensively studied and reviewed.^{3–9} The idiosyncratic behavior of liquid water in particular, such as its negative thermal expansion coefficient below 4 °C, arises from the intricate dynamics of extended hydrogen bond networks that have been investigated numerically, spectroscopically, and by diffraction techniques on picosecond and femtosecond timescales.^{10–16} Intricacies of water structure, such as the dynamic interplay of tetrahedral and ring or chain-like molecular formations and the problem of how the hydrogen bond exists well above its percolation threshold despite its short lifetime in the few picosecond (ps) regime,^{17–19} remain problems that are under active investigation.^{5,20–22} Furthermore, the hydrophobic interaction

of water with biological molecules governs such fundamental aspects as the stability of protein conformations, and DNA structure in solution is an important field of study.^{23,24}

Liquids generally, and water in particular, do not have a structure in the sense of fixed average atomic positions as in the case of solids. Still, they exhibit characteristic spatial and temporal correlations between atomic and molecular centers as governed by intra- and intermolecular forces. These correlations are directly measurable through scattering by short wavelength radiation, most notably x-rays, neutrons, and electrons. The first static electron diffraction study, which determined the radial distribution function, was on gaseous light and heavy water by Ref. 25 in 1965. In 1974, Ref. 26 reported electron diffraction on liquid water, and in a follow-up experiment (Ref. 27), the radial distribution function could be determined with an accuracy comparable to the x-ray and neutron diffraction experiments of the time.^{28,29} In 1994, Ref. 30 reported electron diffraction on vapor-deposited water ice in vacuum during warm-up from 15 K to 188 K, and more recently, electron diffraction

of glassy water under cryo-EM conditions was reported in Ref. 31. Since the 1980s, the x-ray and neutron diffraction experiments and analyses have improved in leaps and bounds, with multiple high precision x-ray measurements becoming available.^{28,32–39} These, combined with neutron diffraction experiments using isotope substitution, allowed separation of the radial distribution function into the oxygen–oxygen (O–O), oxygen–hydrogen (O–H), and hydrogen–hydrogen (H–H) pair distributions. The radial function from x-ray measurements lacks sensitivity to the O–H and H–H correlations, while the neutron diffraction has large systematic errors due to the large probe size,²² but combination of the measurements has yielded high precision O–O pair distributions.⁴⁰ Since electrons as charged particles interact with atomic nuclei via the electrostatic potential associated with each atom as opposed to the interaction of x-rays with electronic polarization and associated electron orbitals, there is no lower limit for the atomic number of atoms acting as electron scatterers.⁴¹ For water, this implies that electron scattering data are sensitive not only to O–O but also to O–H and, in principle, even H–H pair distributions, allowing for a deeper and more direct view of the hydrogen bond structure.

Electron scattering experiments on liquids pose significant experimental challenges, particularly the problem of maintaining, in a high vacuum environment, sufficiently thin liquid layers (about 150 nm for 200 keV electrons in water) that are required to forego multiple scattering events. The latter obscure the oscillations in the acquired radial distribution function from which structural information is extracted. *In situ* growth of thin water films as employed in hydration stages of environmental transmission electron microscopes (TEMs) or achieved through a nozzle based on vacuum deposition is viable but limits experimental conditions to a narrow region of the temperature–pressure phase diagram due to the lack of control over ambient specimen pressure.^{15,42,43} In-vacuum liquid jet technology only partially mitigates such limitations and is significantly more challenging to set up and operate.^{16,44,45}

The use of windowed liquid cell technology, most commonly based on amorphous silicon nitride (Si_3N_4) thin films, has become well established in the field of liquid cell TEM^{43,46–50} and allows for electron based liquid specimen studies under true near-native conditions.^{51–53} Practical current implementations typically demand Si_3N_4 window thicknesses in the range of 20 nm–50 nm in order to avoid window bulging or rupture caused by the pressure differential between the ambient liquid and the vacuum of the TEM column.^{50,54–56} This implies that microscopy and scattering signals are necessarily burdened with a significant background due to the Si_3N_4 window material. Here, we present electron scattering data of liquid water at near-ambient temperature (23 °C) and pressure acquired using a recently developed environmental liquid cell (ELC) setup⁶⁶ that combines standard Si_3N_4 flow cell approaches with windowed environmental cell technology, thus avoiding water layer bulging and enabling the maintenance of ideal layer thicknesses.^{43,49,57} We provide a full analysis methodology of the obtained radial function pertaining to the combined water and Si_3N_4 layers based on the existing x-ray data analysis approaches and include multiple scattering effects. We demonstrate the capability of our method to extract intermolecular O–O and O–H correlations. This opens the door to windowed liquid cell based structural dynamics investigations of hydrogen bond dynamics in water and, more

generally, solution phase chemistry in TEMs and tabletop electron diffractometers.

II. STRUCTURE OF LIQUID WATER

Liquids do not have a structure in the same way that a crystal has a structure as the individual molecules are continually moving around. However, the constituent atoms have well-defined sizes and closest distances of approach, implying that liquids have a definite structure relative to the origin at the center of the average atom. This type of structure is expressed by a radial distribution function $4\pi r^2 g(r)$, where $4\pi r^2 g(r) dr$ is the average number of atom centers between distances r and $r + dr$ from the center of an average atom.

A. Scattering theory

The most convenient quantity to describe the angular distribution of the scattered electrons is the differential cross section and the corresponding mean-free-path length. Electrons that pass through an element of area $d\sigma$ of the parallel incident beam area will be scattered into a cone of solid angle $d\Omega$. The differential cross section, $d\sigma/d\Omega$, is a function of the momentum transfer $Q = 4\pi \sin(\theta/2)/\lambda$, with the scattering angle θ and the electron wavelength λ .

The cross section oscillates around the scattering of N independent atoms without interference, $A(Q)$,

$$\frac{1}{N} \frac{d\sigma}{d\Omega} = A(Q) + B(Q) \int_0^\infty 4\pi r^2 \rho [g(r) - 1] \frac{\sin(Qr)}{Qr} dr, \quad (1)$$

with a weighing factor for the oscillations, $B(Q)$, and the average number density of the sample, ρ . The choice of the weighing factor, $B(Q)$, is arbitrary, but without it, the structure factor would only show the correlations between electrons and the nucleus and not between the atoms.⁵⁸ In x-ray diffraction, Eq. (1) was first derived by Ref. 59 and applied by Ref. 60 on liquid mercury. A detailed derivation is given by Ref. 61.

There are many different ways of defining $A(Q)$ and $B(Q)$ depending on the focus of the investigation. We will use two schemes, the atomic and molecular.⁴⁰ In the atomic scheme, we subtract only the self-scattering and the incoherent scattering of the atoms, defined as

$$A_{at}(Q) = \sum_{\alpha} c_{\alpha} f_{\alpha}^2(Q) + \sum_{\alpha} c_{\alpha} S_{\alpha}(Q). \quad (2)$$

Here, the sum runs over the different species (α) in the sample, with the electron coherent scattering factor, $f_{\alpha}(Q)$, the incoherent scattering factor, $S_{\alpha}(Q)$, and the atomic concentration, c_{α} . The weighing factor, $B(Q)$, is given by

$$B(Q) = \left[\sum_{\alpha} c_{\alpha} f_{\alpha} \right]^2, \quad (3)$$

representing the electron scattering without interference. For the molecular scheme, the intra-molecular interference is also subtracted, so $A(Q)$ is constructed using the independent atom

approximation or the Debye model,

$$A_{mol}(Q) = \sum_{ij} f_i(Q) f_j(Q) \frac{\sin(Qr_{ij}) e^{-b_{ij}Q^2}}{Qr_{ij}} + \sum_{\alpha} c_{\alpha} S_{\alpha}(Q), \quad (4)$$

with the Debye–Waller factor, $b_{i,j}$, and the molecular bond lengths $r_{i,j}$ between atoms i and j . The atomic or molecular structure factor is defined as

$$S_{at/mol}(Q) - 1 = \left(\frac{1}{N} \frac{d\sigma}{d\Omega} - A_{at/mol}(Q) \right) / B(Q). \quad (5)$$

The relationship in Eq. (1) can be inverted using a Fourier transform connecting the structure factor with the radial distribution function,

$$g_{at/mol}(r) = 1 + \frac{1}{2\pi^2 r \rho} \int_0^{\infty} Q (S_{at/mol}(Q) - 1) \sin(Qr) dQ. \quad (6)$$

The structure factor of water can also be decomposed into the individual contributions of the different bond lengths,

$$S_{at/mol}(Q) = w_{OO} S_{OO} + w_{OH} S_{OH} + w_{HH} S_{HH}, \quad (7)$$

with the weighing factors defined as

$$w_{OO} = \frac{f_O^2(Q)}{9B(Q)}, w_{OH} = \frac{4f_O(Q)f_H(Q)}{9B(Q)}, w_{HH} = \frac{4f_H^2(Q)}{9B(Q)}. \quad (8)$$

The partial structure factors can then be individually transformed into the pair distributions g_{OO} , g_{OH} , and g_{HH} . The decomposition requires different datasets, since the x-ray measurements and electron measurements on their own do not distinguish between the atoms. Conversely, the neutron experiments using isotope substitution can distinguish. Hence, the neutron data are usually combined with the x-ray experiments to obtain a high precision g_{OO} pair distribution.⁴⁰

Comparing the different bond length weights in Fig. 1 shows why x-ray scattering is insensitive to the oxygen–hydrogen bond length as it only contributes about 20% of the signal from 0 Å to around 5 Å after which it drops away.

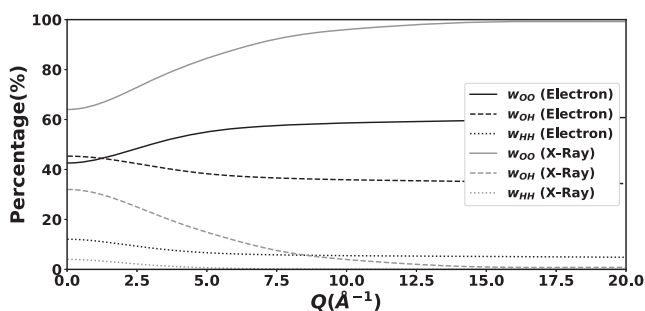


FIG. 1. Comparison of the bond-length weights of x-ray and electron scattering. The electron weight (black lines) of the oxygen–oxygen bond length (solid line) contributes 40% of the signal for small Q and then increases to 60% around 4 Å, the point at which the oxygen–hydrogen bond contribution decreases. The x-ray weights (gray lines) exhibit the same behavior, where the oxygen–oxygen bond length (solid line) contributes 60% at small Q , which increases to nearly 100% at Q values larger than 4 Å. In the x-ray case, the hydrogen–hydrogen bond length is about a 0.5% and for electrons about 6%.

B. Multiple-scattering effects

In practice, multiple scattering has to be taken into account for all but the thinnest samples. For an example with carbon films, see Ref. 62, and for the relation with the Moliere formula, see Ref. 63. Assuming that the scattering is concentrated to small angles $Q \approx 2\pi\theta/\lambda$, we normalize the form factors by dividing with the total scattering,

$$\sigma = \frac{\lambda^2}{4\pi^2} \int_0^{\infty} 2\pi A(Q) Q dQ, \quad (9)$$

giving

$$A_1(Q) = \frac{\lambda^2}{4\pi^2 \sigma} A(Q). \quad (10)$$

The total scattering is related to the mean-free-path length with $\Lambda = 1/(\rho\sigma)$.

The angular distribution for n scattering events is given by n two-dimensional convolutions of the single scattering distribution, $A_1(Q)$, with itself,⁴¹

$$A_n(Q) = A_{n-1}(Q) \otimes A_1(Q). \quad (11)$$

Weighing all the possible number of scattering events with the probability of them occurring gives the multiple scattering form factor,

$$A^*(x, Q) = \exp(-x/\Lambda) \sum_{n=1}^{\infty} (x/\Lambda)^n A_n(Q) / n!, \quad (12)$$

which depends on the thickness of the sample, x . We can then rewrite Eq. (1) to account for multiple scattering,

$$\frac{4\pi^2}{\lambda^2 I_0} \frac{dI_{exp}}{d\Omega} = \sigma_A A^*(x, Q) + \sigma_B B^*(x, Q) \times \int_0^{\infty} 4\pi r^2 \rho [g(r) - 1] \frac{\sin(Qr)}{Qr} dr, \quad (13)$$

with the intensity observed in the detector, I_{exp} , the incident current, I_0 , and the multiple scattering version of the weighing factor, $B^*(x, Q)$. The multiple scattering version of the structure factor is

$$S(Q) - 1 = \left(\frac{4\pi^2}{\lambda^2 I_0} \frac{dI_{exp}}{d\Omega} - \sigma_A A^*(x, Q) \right) / (\sigma_B B^*(x, Q)). \quad (14)$$

The construction of the multiple scattering normalization factor, $B(Q)$, is similar to the construction of $A(Q)$. The multiple scattering expression [Eq. (12)] is applied to $B(Q)$ with the mean-free-path of the elastic component of $A(Q)$ so that $B(Q)$ is used as a reference wave. This division in the diffraction space is equivalent to a deconvolution in real-space and should remove the multiple scattering effects from the radial distribution function.

C. Numerical implementation and Fourier transforms

The numerical implementation, especially of the Fourier transforms in the analysis, requires some care. For the multiple convolutions in Eq. (12), we rewrite the formula in terms of the two-dimensional Fourier transforms of the scattering factors,

$$\tilde{A}^*(t_x, t_y) = \int_0^{\infty} \int_0^{\infty} A(Q_x, Q_y) e^{it_x Q_x + it_y Q_y} dQ_x dQ_y, \quad (15)$$

writing \tilde{f} for the Fourier transform of f , which gives

$$\tilde{A}^*(t_x, t_y) = \exp(-x/\Lambda) [\exp(\tilde{A}(t_x, t_y)x/\Lambda) - 1]. \quad (16)$$

It is possible to replace the two-dimensional Fourier transform in Eq. (15) with a one-dimensional Hankel transform by using projected distributions,⁶⁴ but even custom numerical integration codes struggle with the Hankel transform, so we stick with the two dimensional Fourier transform. The theoretical values of $A(Q)$ are interpolated and sampled every 0.01 Å in a 4096 × 4096 grid. The Fast Fourier Transform (FFT) of the grid is taken, and the formula,

$$\tilde{A}^*(t_x, t_y) = \exp(-x/\Lambda) [\sinh(\tilde{A}(t_x, t_y)x/\Lambda)] + (\cosh(\tilde{A}(t_x, t_y)x/\Lambda) - 1)\phi(t_x, t_y), \quad (17)$$

with the phase mask $\phi(t_x, t_y) = e^{i\pi(t_x+t_y)}$ is applied. The even and uneven terms are split because the FFT performs a circular convolution, and the even terms require a phase shift to align with the uneven terms. The radial average of the inverse FFT is taken to give the multiple scattering distribution.

The second part of the analysis that requires a Fourier transform is the transformation of the structure factor. The difficulty in this case is that the data have limited support between Q_{\min} and Q_{\max} , which causes spurious oscillations in the radial distribution function. The problem is treated by multiplying the structure factor with a modification function before transformation. We use a discrete sampling function, the sinc function or Lorch function as the modification function,⁶⁵

$$M(Q) = \text{sinc}(Q/Q_{\max}) = \frac{\sin(\pi Q/Q_{\max})}{\pi Q/Q_{\max}}, \quad (18)$$

which compensates for the truncation of high Q -values of the data in the transform,

$$\rho_{at/mol}(r) - 1 = \frac{1}{2\pi^2 r \rho_\alpha} \int_{Q_{\min}}^{Q_{\max}} Q(S_{at/mol}(Q) - 1) \times \sin(Qr)M(Q)dQ. \quad (19)$$

No adjustments were done for the truncation of low Q -values.

III. ELECTRON DIFFRACTION ON LIQUID WATER

In order to realize a thin (135 nm), stable, and uniform water film for acquiring the electron scattering data, we used an in-house developed environmental liquid cell (ELC) assembly and method, the technical details of which will be published elsewhere.⁶⁶ The above-mentioned ELC setup incorporates silicon nitride (Si_3N_4) flow-cell technology with a design based on that of Ref. 49, which was subsequently also utilized in Refs. 52 and 53. In its present implementation, the flow cell structure comprises a pair of free-standing rectangular ($30 \times 100 \mu\text{m}^2$) (Si_3N_4) windows with a nominal thickness of 20 nm on $3 \times 8 \text{mm}^2$ rectangular silicon (Si) chips, which incorporate a channel with inlet and outlet ports for directed liquid or gas flow through the Si_3N_4 window region. The $\text{Si}_3\text{N}_4/\text{Si}$ chips have been fabricated to our design and specifications by SimPore, USA.

The ELC setup was prepared by drop casting 1 μl of deionized water on one of the $\text{Si}_3\text{N}_4/\text{Si}$ chips, placing a custom-shaped 10 μm thick polyimide (Kapton) spacer onto it and capping the assembly with the second $\text{Si}_3\text{N}_4/\text{Si}$ chip, whereupon the resulting sandwich with a 10 μm thick windowed flow channel was enclosed and sealed in our custom-built ELC sample transfer arm. A custom-built humid air pressure and flow regulator based on the system of Ref. 57 and in greater detail elsewhere (Ref. 66) was connected to the inlet and outlet of the ELC sample transfer arm for the electron scattering measurements.

All scattering data were collected on a JEOL JEM-2100 transmission electron microscope operated at 200 kV and fitted with a TVIPS TemCam F216 camera. Darkfield and flatfield calibrations were done on the camera prior to measurements, and the camera length was calibrated using diffraction rings from a polycrystalline aluminum film. The electron spot size for diffraction was 12.4 μm as set by the condenser aperture without inserting a selected area aperture, and the dose rate was determined to be $0.09 \pm 0.01 e^-/\text{\AA}^2$ as measured from the current density readout of the JEOL JEM-2100 phosphor screen. All diffraction patterns were recorded with an exposure time of 1 s and an effective camera length of 33.3 cm. Inline layer thickness monitoring was realized by recording pairs of real space images and determining their total image intensity counts I and I_0 , corresponding to cases with and without an objective aperture (half angle of acceptance $\theta = 12.6 \text{ mrad}$) inserted. The corresponding intensity ratio I/I_0 was used to compute thickness estimates of water and Si_3N_4 by the log ratio method using scattering models and material parameters as described below.^{41,57,67}

After inserting the ELC transfer arm and basic alignments, the relative pressure was set to 400 mbar and a flow rate of 30 ml/min was applied to remove the water layer from the Si_3N_4 windows as confirmed by measuring the scattering intensity ratio $I/I_0 = 0.88 \pm 0.01$ corresponding to $24 \pm 2 \text{ nm}$ thickness in the atomic scattering model. Twenty diffraction images of the exposed Si_3N_4 window (without water) were recorded, whereupon the flow rate was reduced to about 1 ml/min and adjusted until a stable scattering ratio of $I/I_0 = 0.70 \pm 0.02$ was observed, corresponding to $160 \pm 20 \text{ nm}$ of water thickness in the atomic scattering model. Another 20 diffraction images were recorded under these conditions for further analysis. The beam block was masked out, the center determined by fitting a Lorentzian, and the radial average and variance were taken around this center, giving a Q range of $0.83 \text{ \AA}^{-1} - 17.4 \text{ \AA}^{-1}$, which is transformed to a real space range of 0 $\text{\AA} - 17 \text{ \AA}$.

A. Diffraction data from silicon nitride

The inelastic scattering of electrons is related to the x-ray incoherent scattering factors $F_i(Q)$ by

$$f_i(Q) = \frac{4}{a_H^2} \frac{F_i(Q')}{Q'^4} \quad (20)$$

with $Q'^2 = Q^2 + Q_E^2$, where Q_E is the average momentum transfer to the sample,

$$Q_E = \frac{2\pi}{\lambda} \frac{\Delta E}{E} \frac{E + E_0}{E + 2E_0}, \quad (21)$$

with E_0 being the rest energy of the electron and E being the acceleration voltage. Following the suggestion of Ref. 68, we set ΔE equal to half the binding energy of the molecule, $\Delta E = J/2$, with $J = 13.6Z$. The subsequent analysis is robust to moderate changes in the value of ΔE as it only shifts the inelastic scattering form factor, which is mostly concentrated on small Q -values, on the Q -axis. The effective atomic number of silicon nitride is taken as 10.6, the atomic weight is taken as 20 g/mol, and the density is taken as 3.17 g/cm³. The atomic scattering factor and normalization factor are constructed from the elastic form factors given in Ref. 69 and the inelastic x-ray form factors given in Ref. 70,

$$A_{\text{SiN}}(Q) = \frac{3}{7}[S_{\text{Si}}(Q) + f_{\text{Si}}^2(Q)] + \frac{4}{7}[S_{\text{N}}(Q) + f_{\text{N}}^2(Q)], \quad (22)$$

$$B_{\text{SiN}}(Q) = \left[\frac{3}{7}f_{\text{Si}}(Q) + \frac{4}{7}f_{\text{N}}(Q) \right]^2. \quad (23)$$

The mean-free-path lengths of silicon nitride can then be calculated to be 96 nm, 69 nm, and 40 nm for the elastic, inelastic, and total scattering, respectively. The multiple scattering version is computed from $A_{\text{SiN}}(Q)$ and $B_{\text{SiN}}(Q)$ and the known silicon nitride thickness of 25 nm as measured by a parallax method.

The experimental data are fitted to the theoretical model by minimizing the fit function,

$$\left[\frac{a_0 I_{\text{exp}}(Q) - a_1 - a_2/Q - A_{\text{SiN}}^*(x, Q)}{B_{\text{SiN}}^*(x, Q) \delta I_{\text{exp}}(Q)} \right]^2, \quad (24)$$

with the experimental data $I_{\text{exp}}(Q)$ and experimental error $\delta I_{\text{exp}}(Q)$. The fitting contains an electron dose scaling, a_0 , which is different for each micrograph and two polynomial constants, a_1 and a_2 , to compensate for dark current and non-linear effects in the camera response and is kept the same for all the micrographs. The standardized data are then added together using a weighted mean with the inverse variance as the weight. Half the square of the polynomial is added to the variance in each bin as an estimate of the systematic error. The atomic model does not contain any interference effects, and thus, discrepancies for small Q are to be expected and can be seen in Fig. 2. Subtracting the atomic model and dividing with the normalization factor gives the atomic structure factor of silicon nitride. In the left panel of Fig. 3, we plot the modified structure factor

$$S'(Q) - 1 = [S^*(Q) - 1]M(Q), \quad (25)$$

to emphasize which errors contribute to the radial distribution function. The modified structure factor is then transformed using the discrete version of Eq. (19) to find the atomic radial distribution of silicon nitride,

$$g_{\text{SiN}}(r) - 1 = \sum_{Q=Q_{\text{min}}}^{Q_{\text{max}}} \frac{1}{2\pi^2 r \rho} Q(S'(Q) - 1) \sin(Qr) \delta Q, \quad (26)$$

with δQ being the bin size, and the errors are computed using the corresponding error propagation formula,⁷¹

$$(\delta g_{\text{SiN}}(r))^2 = \sum_{Q=Q_{\text{min}}}^{Q_{\text{max}}} \left(\frac{\sin(Qr)}{2\pi^2 r \rho} Q(\delta S'(Q) - 1) \delta Q \right)^2, \quad (27)$$

where $\delta S'(Q)$ is the error in the structure factor. The atomic radial distribution of silicon nitride is plotted in the right-hand side panel

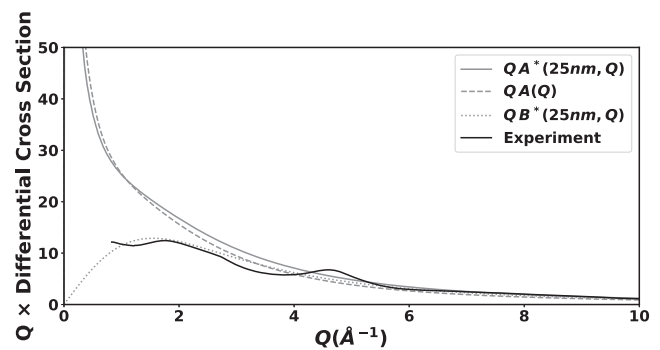


FIG. 2. Comparison of the theoretical model without multiple scattering, $A(Q)$, the multiple scattering model, $A^*(Q)$, and the normalization factor, $B^*(Q)$, with the experimental data, $I_{\text{exp}}(Q)$, after fitting. All the quantities have been multiplied by Q to emphasize the shape of the distributions. Given that the thickness of the silicon nitride is 25 nm and the mean-free-path-length is 40 nm, the multiple scattering effects are not excessive, but it does thicken the tails of the distribution, which does have a large effect on the fitting of the data.

of Fig. 3. The r lattice is sampled from 0 Å to 17 Å in increments of 0.05 Å. This result can be compared to the similar x-ray measurement in Ref. 72, where the Si–N correlation was seen at 1.75 Å and the N–N and Si–Si bonds lengths at 3.00 Å. The peaks observed at 1.70 Å and 2.95 Å are quite a decent correspondence. We have written $C_{\text{SiN}}(Q)$ for the diffraction measurement extended to smaller and larger Q by transforming the radial distribution back to the diffraction space and adding it to the model.

B. Diffraction from water and silicon nitride combined at room temperature

The analysis of the filled liquid cell requires the combination of a silicon nitride and water layer. For water, we do not use the independent atom model to construct the molecular scattering factor,

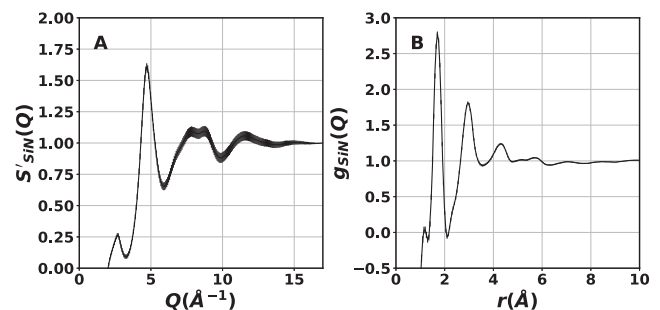


FIG. 3. (a) The modified atomic structure factor of silicon nitride with error. (b) The corresponding atomic radial distribution of silicon nitride. For $Q < 1 \text{ \AA}^{-1}$, there is a sharp unphysical drop corresponding to errors in the theoretical model; fortunately, there are no bond lengths in this region, and we can resolve the Si–N correlations at 1.7 Å with a height of 2.78, the N–N and Si–Si bond lengths combine at 2.95 Å with a height of 1.81 and the Si–N–Si and N–Si–N bond lengths combine at 4.3 Å with a height of 1.24.

since a quantum mechanics calculation using configuration interaction wavefunctions is available in the literature.⁷³ Writing $C_{\text{H}_2\text{O}}(Q)$ for the combined elastic and inelastic scattering factor from Ref. 73 and $C_{\text{SiN}}(Q)$ for the measured silicon nitride scattering factor, each scattering factor is transformed into its multiple scattering version and added together in the Fourier space,

$$\tilde{C}_{\text{H}_2\text{O}+\text{SiN}} = c_{\text{SiN}}\tilde{C}_{\text{H}_2\text{O}} + \tilde{C}_{\text{SiN}}c_{\text{H}_2\text{O}} + \tilde{C}_{\text{SiN}}\tilde{C}_{\text{H}_2\text{O}}, \quad (28)$$

with $c_{\text{H}_2\text{O}}$ for the probability to not scatter in the water layer and c_{SiN} to not scatter in the silicon nitride layer. For the normalization factor, the effects of the hydrogen and water components need to be separated, and in the x-ray analysis, the atomic scattering factors are transformed using the equation from Ref. 74,

$$f'_{X,\alpha}(Q) = f_{X,\alpha}(Q) \left[1 - \frac{a_\alpha}{z_\alpha} \exp(-Q^2/2\delta^2) \right], \quad (29)$$

for atom species α , which could be transformed to the electron scattering factors using the Mott–Bethe formula,⁶⁹

$$f'_e(Q) = \frac{2}{a_o} \left[\frac{Z - f'_X(Q)}{Q^2} \right]. \quad (30)$$

The purpose of the transformation is to account for, in the individual form factors, the charge redistribution that occurs when the hydrogen forms a covalent bond with the oxygen atom. For the electron scattering, we do not use this formula as it significantly degrades our results, but for the x-ray scattering factors, we set the parameters to the same as in Ref. 74, $a_{\text{H}} = 1/3$, $a_{\text{O}} = 2/3$, and $\delta = 2.2$ corresponding to a third of a charge moving from the hydrogen to the oxygen atom. The normalization factor is constructed by

$$B_{\text{H}_2\text{O}} = \left[\frac{1}{3}f_{\text{O}}(Q) + \frac{2}{3}f_{\text{H}}(Q) \right]^2, \quad (31)$$

and the same procedure is applied to the normalization factor as in Eq. (17) to construct $B_{\text{H}_2\text{O}}^*$ and Eq. (28) for $B_{\text{H}_2\text{O}+\text{SiN}}^*$.

For water, we use the effective Z as 4.69, the density as 0.997 g/cm³, and the mean atomic weight per nucleus as 6 g/mol. The mean-free-path length for water is calculated to be 436 nm, 230 nm, and 151 nm for the elastic, inelastic, and total, respectively. The data are fitted to the model by minimizing the loss function again, but in this case, the exact thickness of the water layer is unknown, which is the largest source of uncertainty for the final result. The different measured diffraction patterns are again added together using a weighted mean, with the weight given by the inverse variance. Half the square of the polynomial is added to the variance in each bin as an estimate of the systematic error. Setting the water thickness to 135 nm minimizes the structure below 1 Å in the radial distribution function (Fig. 4).

The structure factor and the corresponding radial distribution function are compared in Fig. 5 with the averaged x-ray data from Ref. 58 (Normalization IV). In the electron structure factor, the first double peak between 2 Å⁻¹ and 3 Å⁻¹ is suppressed and the dip at 6 Å⁻¹ is not as deep as compared to the x-ray data. The difference can be explained by the increased sensitivity of electron diffraction to the hydrogen–oxygen bond length. In panel B, the radial distribution of the x-ray experiments is compared to our electron diffraction experiment. To compare the measured radial function with theory,

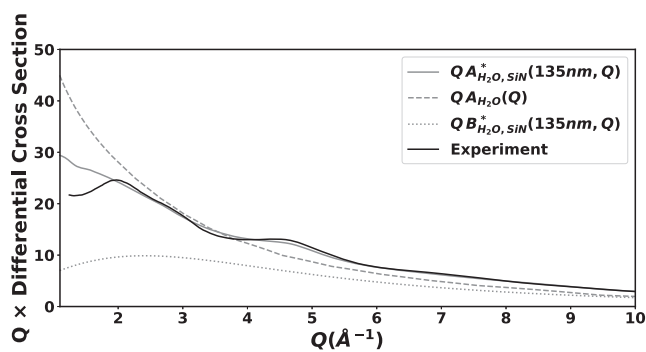


FIG. 4. Comparison of the theoretical model of water scattering, $A_{\text{H}_2\text{O}}(Q)$, the multiple scattering model with the silicon nitride layer, $A_{\text{H}_2\text{O},\text{SiN}}^*(Q)$, and the normalization factor, $B^*(Q)$, with the experimental data, $I_{\text{exp}}(Q)$, after fitting. The water layer is 135 nm with a mean-free-path of 151 nm combined with the silicon nitride layer of 25 nm with a mean-free-path of 40 nm. The additional nitride layer does change the shape of the scattering significantly. The normalization factor, $B^*(135 \text{ nm}, Q)$, is also plotted, and all the distributions have been multiplied with Q to emphasize their shapes.

we transform the theoretical pair distributions to scattering oscillations and weigh them with the pair bond weights [Eq. (8)] and then transform them back. The theoretical pair distributions are from the Empirical Potential Structure Refinement (EPRS) of Ref. 58, which is a reverse Monte Carlo simulation with an empirical potential constrained by the known physical ranges of the bond lengths and the x-ray and neutron datasets. The normalization of the EPRS peaks was changed from II to IV using the definitions of Ref. 58 to match our normalization.

In Fig. 6(a), the EPRS oxygen–oxygen peak is at 2.79 Å with a height of 2.50, while the measured peak is at 2.84 Å with a height of 2.21, showing good agreement. The lower measured peak could be due to the modification factor and/or the deconvolution not completely removing all the multiple scattering, both effects that lead to

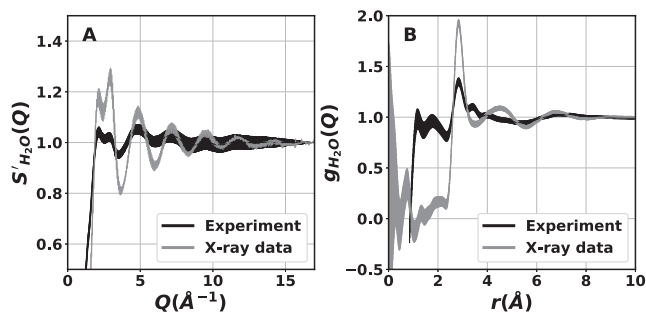


FIG. 5. (a) Comparison between the experimentally measured structure factor and the merged x-ray data from Ref. 58. (b) The corresponding radial distributions. Below 0.8 Å, there is an unphysical drop in our radial distribution probably caused by our fitting procedure and the unknown silicon nitride scattering. At 1.8 Å, the O–H bond length can clearly be seen in our radial function, while it is suppressed in the x-ray experiment.

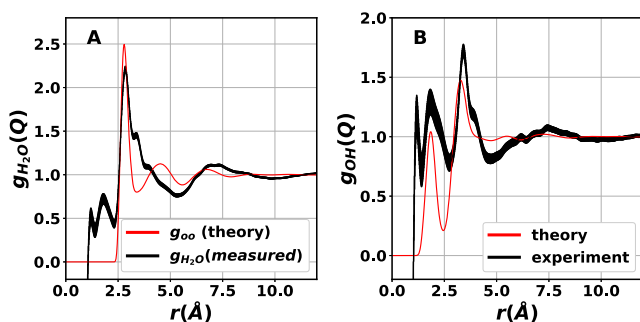


FIG. 6. (a) The experimental water radial distribution is multiplied with the x-ray oxygen weight and compared with the EPRS oxygen contribution. The EPRS oxygen–oxygen peak is at 2.79 Å with a height of 2.50 compared to the measured peak at 2.84 Å with a height of 2.21. (b) Comparison between the experimental radial distribution function with the oxygen–oxygen pair distribution subtracted and the residue divided by the oxygen–hydrogen weights before transformation. The EPRS oxygen–hydrogen peaks are at 1.86 and 3.27 with heights of 1.04 and 1.48, respectively, while the measured peaks are at 1.83 and 3.41 with heights 1.29 and 1.72, respectively. The measured peak heights are consistently higher than the theory due to our naive separation procedure.

a reduction in height and broadening of the peaks. A peak corresponding to the intramolecular oxygen–hydrogen bond, which was not completely subtracted with the molecular scattering factor, is observed at 1.1 Å. The additional structure at 1.8 Å and 3.4 Å is due to the intermolecular oxygen–hydrogen bond contribution.

The oxygen–oxygen pair distribution is subtracted from the measurement, divided by the oxygen–hydrogen weight and transformed to find the experimental oxygen–hydrogen pair distribution. The measured and theoretical oxygen–hydrogen pair distribution are compared in Fig. 6(b). The EPRS oxygen–hydrogen peaks are at 1.86 and 3.27 with heights of 1.04 and 1.48, respectively, while the measured peaks are at 1.83 and 3.41 with heights 1.29 and 1.72, respectively. Note that we did not use the parametrization of Ref. 74 [Eq. (29)] as the peak height varies greatly depending on the parameters used. Our simplistic separation procedure systematically over estimates the baseline resulting in the peak height being consistently larger than the theory in Fig. 6(b) and also reduces the dip at 1.83 Å–3 Å. The additional oxygen–hydrogen peak is still present at 1.1 Å, and a much stronger dip is observed at 5 Å, which requires further investigation. For a more exact separation of the pair distributions and distinguishing the hydrogen–hydrogen pair distribution from the oxygen–hydrogen pair distribution, a more suitable parametrization and an analysis akin to EPRS for electron scattering are needed.

IV. POSSIBLE STRUCTURE OF WATER FROM THE RADIAL DISTRIBUTION FUNCTION

The pair distribution functions obtained from the scattering data contain information about intra- and intermolecular bonds averaged over the time of acquisition. The structure of liquid water can be characterized by the number of bonds that a water monomer can form with its neighbors, which can be extracted from the pair

distribution functions. The hydrogen bond lengths in water are flexible, which is why the corresponding oxygen–hydrogen and oxygen–oxygen peaks are broad.⁷⁵

The number of β -type atoms around an α -type atom at the origin would be given by the coordination number,⁵⁸

$$N_{\alpha\beta} = 4\pi\rho_{\beta} \int_{r_{\min}}^{r_{\max}} r^2 g_{\alpha\beta}(r) dr. \quad (32)$$

For the oxygen–oxygen coordination number, we divide the structure factor with the oxygen–oxygen weight and transform to the radial function, which we integrate from 2.34 Å to 3.36 Å to isolate the oxygen–oxygen peak,

$$N_{OO} = 4.80 \pm 0.15. \quad (33)$$

Note that the structure factor of water was used, so the integration range still contains some contribution from the oxygen–hydrogen bond causing an over estimation. X-ray experiments and molecular dynamic (MD) simulations give the intermolecular oxygen–oxygen effective bond length as 2.82 Å with coordination number 4.67 ± 0.01 .^{58,75,76} We observe the oxygen–oxygen bond length as 2.84 Å with a larger coordination number, implying about 1% error in calibration and a systematic error of about 3% due to our simplistic pair distribution separation.

Subtracting the oxygen–oxygen pair distribution from the radial distribution and integrating from 1.41 Å to 2.34 Å to isolate the first oxygen–hydrogen peak related to the degree of hydrogen bonding gives

$$N_{OH} = 2.53 \pm 0.35. \quad (34)$$

Neutron scattering data give the oxygen–hydrogen bond length as 1.85 Å with coordination number 1.88 ± 0.06 .^{58,77} We observe the peak at 1.83 Å but with a much larger coordination number. The EPRS oxygen–oxygen pair distribution does not exactly match what we observe and simply subtracting it causes a systematic error in the baseline, but it does confirm that we observe the intermolecular hydrogen–oxygen bond length. The theoretical resolution of the radial distribution is coupled to the maximum Q used in the Fourier transform, and in our case, $Q_{\max} = 17 \text{ \AA}^{-1}$ so that the resolution is $2\pi/Q_{\max} = 0.37 \text{ \AA}$, explaining why we observe the oxygen–hydrogen peak, while Ref. 16 only observed a shoulder at 1.8 Å ($Q_{\max} = 10 \text{ \AA}$).

Taking the coordination number at a face value implies the number of hydrogen bonds per water molecule to be 5 ± 0.7 ,⁷⁸ which is more than the values reported by Ref. 79 (3.9) and Ref. 80 (3.1).⁸¹

V. CONCLUSION

The work presented here highlights a simple tabletop approach using a novel ELC concept for performing static diffraction measurements on liquids, water in this case. This method can easily be extended to enable time resolved diffraction studies of reaction dynamics or real space applications to take advantage of the liquid environment to simultaneously image structures and dynamics. This latter feature will be particularly interesting for studies of biological macromolecules and assemblies. Furthermore, a novel analysis protocol for removing the contribution of silicon nitride windows, the

main bottleneck in such experiments, has been introduced. Compared to the previous electron diffraction studies on water, the ELC is capable of producing a repeatable thin water layer, which allows image acquisition for a longer time. Consequently, the information extracted from the radial distribution function for the intermolecular oxygen–oxygen bond matched extremely well to the x-ray scattering measurements and MD simulations, with only 1% error in the obtained bond length, and as electrons are more sensitive to hydrogen than x-rays, we were able to extend the diffraction analysis to obtain a peak at 1.88 Å. This value is in very good agreement with the neutron scattering data as compared to the small shoulder seen at 1.8 Å by Ref. 16.^{58,77} The mismatch in the oxygen–hydrogen coordination number can be attributed to error in the baseline determination, as explained in Sec. IV. It will be important to refine the baseline correction to fully resolve the degree of hydrogen bonding to finally resolve this key feature in understanding the dynamic structure of liquid water. By going to thinner windows, it will be possible to greatly reduce the background and reduce the uncertainty in the background correction to resolve the degree of coordination. Within the present resolution, the coordination numbers and bond lengths are obtained by associated changes in energy partitioning in translational and increased thermal fluctuations and vibrational degrees of freedom on the number of hydrogen bonds per water molecule to give new insight into the dynamic structure of liquid water. In the future, this approach can be utilized to conduct a temperature dependent study on liquid water and assess the effect of increased thermal fluctuations and associated changes in energy partitioning in translational and vibrational degrees of freedom on the number of hydrogen bonds per water molecule—to give new insight into the dynamic structure of liquid water.

SUPPLEMENTARY MATERIAL

See the [supplementary material](#) for the silicon nitride and water experimental data that were used to construct the figures in this article.

AUTHORS' CONTRIBUTIONS

M.B.d.K. and S.A. contributed equally to this work.

ACKNOWLEDGMENTS

The authors thank Djordje Gitaric and Josef Gonschior from the Atomic Resolved Dynamics department and the Machine Physics Scientific Support unit, both at the Max Planck Institute for the Structure and Dynamics of Matter in Hamburg, Germany, for their technical assistance. We also thank the Max Planck Society, Joachim Herz Foundation, and the Natural Sciences and Engineering Research Council of Canada (NSERC) for funding support.

DATA AVAILABILITY

The data that support the findings of this study are available within the article and its [supplementary material](#).

REFERENCES

- H. Ihee, M. Lorenc, T. K. Kim, Q. Y. Kong, M. Cammarata, J. H. Lee, S. Bratos, and M. Wulff, *Science* **309**, 1223 (2005).
- K. Hwan Kim, J. Kim, J. Hyuk Lee, and H. Ihee, *Struct. Dyn.* **1**, 011301 (2014).
- D. Eisenberg and W. Kauzmann, *Science* **166**, 861 (1969).
- F. H. Stillinger, *Science* **209**, 451 (1980).
- O. Mishima and H. E. Stanley, *Nature* **396**, 329–335 (1998).
- I. Ohmine and S. Saito, *Acc. Chem. Res.* **32**, 741 (1999).
- R. Ludwig, *Angew. Chem.* **40**, 1808 (2001).
- T. Head-Gordon and G. Hura, *Chem. Rev.* **102**, 2651 (2002).
- E. Brini, C. J. Fennell, M. Fernandez-Serra, B. Hribar-Lee, M. Lukšič, and K. A. Dill, *Chem. Rev.* **117**, 12385 (2017).
- F. W. Starr, S. Harrington, F. Sciortino, and H. E. Stanley, *Phys. Rev. Lett.* **82**, 3629 (1999).
- C. P. Lawrence and J. L. Skinner, *J. Chem. Phys.* **118**, 264 (2003).
- C.-Y. Ruan, F. Vigliotti, V. A. Lobastov, S. Chen, and A. H. Zewail, *Proc. Natl. Acad. Sci. U. S. A.* **101**, 1123 (2004).
- D. Kraemer, M. L. Cowan, A. Paarmann, N. Huse, E. T. J. Nibbering, T. Elsaesser, and R. J. D. Miller, *Proc. Natl. Acad. Sci. U. S. A.* **105**, 437 (2008).
- U. Ranieri, P. Giura, F. A. Gorelli, M. Santoro, S. Klotz, P. Gillet, L. Paolasini, M. M. Koza, and L. E. Bove, *J. Phys. Chem. B* **120**, 9051 (2016).
- M. Hada, Y. Shigeeda, S.-y. Koshihara, T. Nishikawa, Y. Yamashita, and Y. Hayashi, *J. Phys. Chem. A* **122**, 9579 (2018).
- J. P. F. Nunes, K. Ledbetter, M. Lin, M. Kozina, D. P. DePonte, E. Biasin, M. Centurion, C. J. Crissman, M. Dunning, S. Guillet, K. Jobe, Y. Liu, M. Mo, X. Shen, R. Sublett, S. Weathersby, C. Yoneda, T. J. A. Wolf, J. Yang, A. A. Cordones, and X. J. Wang, *Struct. Dyn.* **7**, 024301 (2020).
- D. L. Nelson, A. L. Lehninger, and M. M. Cox, *Lehninger Principles of Biochemistry* (Macmillan, 2008).
- P. Wernet, D. Nordlund, U. Bergmann, M. Cavalleri, M. Odelius, H. Ogasawara, L.-Å. Näslund, T. Hirsch, L. Ojamäe, P. Glatzel *et al.*, *Science* **304**, 995 (2004).
- J. Liu, X. He, and J. Z. H. Zhang, *Phys. Chem. Chem. Phys.* **19**, 11931 (2017).
- H. E. Stanley and J. Teixeira, *J. Chem. Phys.* **73**, 3404 (1980).
- J. Teixeira, M.-C. Bellissent-Funel, S. H. Chen, and A. J. Dianoux, *Phys. Rev. A* **31**, 1913 (1985).
- K. Amann-Winkel, M.-C. Bellissent-Funel, L. E. Bove, T. Loerting, A. Nilsson, A. Paciaroni, D. Schlessinger, and L. Skinner, *Chem. Rev.* **116**, 7570 (2016).
- Y. Marechal, *The Hydrogen Bond and the Water Molecule: The Physics and Chemistry of Water, Aqueous and Bio-Media* (Elsevier, 2007).
- P. Ball, *Proc. Natl. Acad. Sci. U. S. A.* **114**, 13327 (2017).
- S. Shibata and L. S. Bartell, *J. Chem. Phys.* **42**, 1147 (1965).
- S. Lengyel and E. Kálmán, *Nature* **248**, 405 (1974).
- E. Kálmán, G. Pálkás, and P. Kovács, *Mol. Phys.* **34**, 505 (1977).
- A. H. Narten and H. A. Levy, *J. Chem. Phys.* **55**, 2263 (1971).
- W. E. Thiessen and A. H. Narten, *J. Chem. Phys.* **77**, 2656 (1982).
- P. Jenniskens and D. F. Blake, *Science* **265**, 753 (1994).
- J. B. Souza Junior, G. R. Schleder, F. M. Colombari, M. A. de Farias, J. Bettini, M. van Heel, R. V. Portugal, A. Fazzio, and E. R. Leite, *J. Phys. Chem. Lett.* **11**, 1564 (2020).
- Y. S. Badyal, M.-L. Saboungi, D. L. Price, S. D. Shastri, D. R. Haeflner, and A. K. Soper, *J. Chem. Phys.* **112**, 9206 (2000).
- G. Hura, D. Russo, R. M. Glaeser, T. Head-Gordon, M. Krack, and M. Parrinello, *Phys. Chem. Chem. Phys.* **5**, 1981 (2003).
- R. Hart, C. Benmore, J. Neufeind, S. Kohara, B. Tomberli, and P. Egelstaff, *Phys. Rev. Lett.* **94**, 047801 (2005).
- L. Fu, A. Bienenstock, and S. Brennan, *J. Chem. Phys.* **131**, 234702 (2009).
- C. Huang, K. T. Wikfeldt, D. Nordlund, U. Bergmann, T. McQueen, J. Sellberg, L. G. M. Pettersson, and A. Nilsson, *Phys. Chem. Chem. Phys.* **13**, 19997 (2011).
- V. Petkov, Y. Ren, and M. Suohomel, *J. Phys.: Condens. Matter* **24**, 155102 (2012).
- L. B. Skinner, C. J. Benmore, and J. B. Parise, *J. Phys.: Condens. Matter* **24**, 338001 (2012).

- ³⁹A. K. Soper, *J. Phys. Chem. B* **115**, 14014 (2011).
- ⁴⁰L. B. Skinner, C. Huang, D. Schlesinger, L. G. M. Pettersson, A. Nilsson, and C. J. Benmore, *J. Chem. Phys.* **138**, 074506 (2013).
- ⁴¹L. Reimer and H. Kohl, *Transmission Electron Microscopy: Physics of Image Formation* (Springer, 2008), Vol. 36.
- ⁴²S. W. Hui and D. F. Parsons, *Science* **184**, 77 (1974).
- ⁴³M. J. Williamson, R. M. Tromp, P. M. Vereecken, R. Hull, and F. M. Ross, *Nat. Mater.* **2**, 532–536 (2003).
- ⁴⁴D. P. DePonte, J. T. McKeown, U. Weierstall, R. B. Doak, and J. C. H. Spence, *Ultramicroscopy* **111**, 824 (2011).
- ⁴⁵J. D. Koralek, J. B. Kim, P. Bruza, C. B. Curry, Z. Chen, H. A. Bechtel, A. A. Cordones, P. Sperl, S. Toleikis, J. F. Kern *et al.*, *Nat. Commun.* **9**, 1353 (2018).
- ⁴⁶H. Zheng, R. K. Smith, Y.-W. Jun, C. Kisielowski, U. Dahmen, and A. P. Alivisatos, *Science* **324**, 1309 (2009).
- ⁴⁷N. de Jonge, D. B. Peckys, G. J. Kremers, and D. W. Piston, *Proc. Natl. Acad. Sci. U. S. A.* **106**, 2159 (2009).
- ⁴⁸E. A. Ring and N. de Jonge, *Microsc. Microanal.* **16**, 622 (2010).
- ⁴⁹C. Mueller, M. Harb, J. R. Dwyer, and R. J. D. Miller, *J. Phys. Chem. Lett.* **4**, 2339 (2013).
- ⁵⁰F. M. Ross, “Quantifying electrochemical processes using liquid cell TEM,” in *Liquid Cell Electron Microscopy*, Advances in Microscopy and Microanalysis, edited by F. M. Ross (Cambridge University Press, 2016), pp. 210–236.
- ⁵¹D. B. Peckys, G. M. Veith, D. C. Joy, and N. de Jonge, *PLoS One* **4**, e8214 (2009).
- ⁵²S. Keskin, S. Besztej, G. Kassier, S. Manz, R. Bückler, D. Venegas-Rojas, S. Riekeberg, H. Trieu, A. Rentmeister, and R. Miller, *J. Phys. Chem. Lett.* **6**, 4487 (2015).
- ⁵³S. Besztej, S. Keskin, S. Manz, G. Kassier, R. Bückler, H. Trieu, A. Rentmeister, and R. Miller, *Microsc. Microanal.* **23**, 46 (2017).
- ⁵⁴U. M. Mirsaidov, H. Zheng, Y. Casana, and P. Matsudaira, *Biophys. J.* **102**, L15 (2012).
- ⁵⁵M. Tanase, J. Winterstein, R. Sharma, V. Aksyuk, G. Holland, and J. A. Liddle, *Microsc. Microanal.* **21**, 1629 (2015).
- ⁵⁶D. Venegas-Rojas, S. Keskin, S. Azim, S. Manz, R. J. D. Miller, and H. K. Trieu, *MikroSystemTechnik 2017; Congress* (VDE Verlag, 2017), pp. 1–4.
- ⁵⁷Y. Inayoshi, H. Minoda, Y. Arai, and K. Nagayama, *Micron* **43**, 1091 (2012).
- ⁵⁸A. K. Soper, *ISRN Phys. Chem.* **2013**, 1.
- ⁵⁹F. Zernike and J. A. Prins, *Z. Phys. A: Hadrons Nucl.* **41**, 184 (1927).
- ⁶⁰P. Debye and H. Menke, *Phys. Z* **31**, 797 (1930).
- ⁶¹B. E. Warren, *X-Ray Diffraction* (Courier Corporation, 1990).
- ⁶²R. E. Burge, D. L. Misell, and J. W. Smart, *J. Phys. C: Solid State Phys.* **3**, 1661 (1970).
- ⁶³G. R. Anstis, Z. Liu, and M. Lake, *Ultramicroscopy* **26**, 65 (1988).
- ⁶⁴D. L. Misell and R. E. Burge, *J. Phys. C: Solid State Phys.* **2**, 61 (1969).
- ⁶⁵E. Lorch, *J. Phys. C: Solid State Phys.* **2**, 229 (1969).
- ⁶⁶S. Azim, L. A. Bultema, M. de Kock, E. R. Osorio-Blanco, M. Calderón, J. Gonschior, J.-P. Leimkohl, F. Tellkamp, R. Bückler, E. C. Schulz, S. Keskin, N. de Jonge, G. Kassier, and R. D. Miller, *Microsc. Microanal.* (submitted) (2020).
- ⁶⁷H. Zhang, R. Egerton, and M. Malac, *Microsc. Microanal.* **16**, 344 (2010).
- ⁶⁸H. Koppe, *Z. Phys. A: Hadrons Nucl.* **124**, 658 (1948).
- ⁶⁹E. J. Kirkland, *Advanced Computing in Electron Microscopy* (Springer Science & Business Media, 2010).
- ⁷⁰J. H. Wang, R. P. Sagar, H. Schmidler, and V. H. Smith, *At. Data Nucl. Data Tables* **53**, 233 (1993).
- ⁷¹T. Weitkamp, J. Neufelnd, H. E. Fischer, and M. D. Zeidler, *Mol. Phys.* **98**, 125 (2000).
- ⁷²T. Aiyama, T. Fukunaga, K. Niihara, T. Hirai, and K. Suzuki, *J. Non-Cryst. Solids* **33**, 131 (1979).
- ⁷³J. Wang, A. N. Tripathi, and V. H. Smith, Jr., *J. Chem. Phys.* **101**, 4842 (1994).
- ⁷⁴J. M. Sorenson, G. Hura, R. M. Glaeser, and T. Head-Gordon, *J. Chem. Phys.* **113**, 9149 (2000).
- ⁷⁵T. E. Gorelik, R. Neder, M. W. Terban, Z. Lee, X. Mu, C. Jung, T. Jacob, and U. Kaiser, *Acta Crystallogr., Sect. B: Struct. Sci., Cryst. Eng. Mater.* **75**, 532 (2019).
- ⁷⁶T. Todorova, A. P. Seitsonen, J. Hutter, I.-F. W. Kuo, and C. J. Mundy, *J. Phys. Chem. B* **110**, 3685 (2006).
- ⁷⁷A. K. Soper and M. G. Phillips, *Chem. Phys.* **107**, 47 (1986).
- ⁷⁸A. Soper and C. Benmore, *Phys. Rev. Lett.* **101**, 065502 (2008).
- ⁷⁹P. D. Fleming and J. H. Gibbs, *J. Stat. Phys.* **10**, 351 (1974).
- ⁸⁰W. T. King and R. E. Barletta, *J. Chem. Phys.* **67**, 180 (1977).
- ⁸¹A. Geiger, F. H. Stillinger, and A. Rahman, *J. Chem. Phys.* **70**, 4185 (1979).